

# Nanoscale

Accepted Manuscript

This article can be cited before page numbers have been issued, to do this please use: Z. Sun, Y. Nakamura, K. Okamoto, S. Izawa, H. Funakubo and Y. Majima, *Nanoscale*, 2025, DOI: 10.1039/D5NR04010H.



This is an Accepted Manuscript, which has been through the Royal Society of Chemistry peer review process and has been accepted for publication.

Accepted Manuscripts are published online shortly after acceptance, before technical editing, formatting and proof reading. Using this free service, authors can make their results available to the community, in citable form, before we publish the edited article. We will replace this Accepted Manuscript with the edited and formatted Advance Article as soon as it is available.

You can find more information about Accepted Manuscripts in the [Information for Authors](#).

Please note that technical editing may introduce minor changes to the text and/or graphics, which may alter content. The journal's standard [Terms & Conditions](#) and the [Ethical guidelines](#) still apply. In no event shall the Royal Society of Chemistry be held responsible for any errors or omissions in this Accepted Manuscript or any consequences arising from the use of any information it contains.

## ARTICLE

High-Resistance-State Tunneling in 25 nm TiO<sub>x</sub>/Y-Doped HfO<sub>2</sub>/Pt Nanocrossbar Ferroelectric Tunnel Junctions<sup>†</sup>Received 00th January 20xx,  
Accepted 00th January 20xx

DOI: 10.1039/x0xx00000x

Zhongzheng Sun,<sup>a</sup> Yoshiko Nakamura,<sup>b</sup> Kazuki Okamoto,<sup>b</sup> Seiichiro Izawa,<sup>a</sup> Hiroshi Funakubo,<sup>b</sup> and Yutaka Majima<sup>\*a</sup>

We report nanocrossbar-type ferroelectric tunnel junctions (FTJs) with a Ti/TiO<sub>x</sub>/7% yttrium-doped HfO<sub>2</sub> (YHO<sub>7</sub>)/Pt structure integrated on thermally oxidized Si substrates, which exhibit clear direct tunneling conduction even in the high-resistance state (HRS) and a tunneling electroresistance ratio exceeding 10<sup>3</sup>. The nanocrossbar FTJs were fabricated using a double-exposure electron-beam lithography (EBL) process with lateral dimensions scaled down to 25 nm. The temperature dependence of the TER effect measurements at 9 and 300 K confirms that both low- and high-resistance states are dominated by the direct tunneling conduction. A maximum TER ratio of  $2.2 \times 10^3$  was obtained in a 3 nm-thick YHO<sub>7</sub> nanocrossbar FTJ with an effective area of  $26 \times 24$  nm<sup>2</sup>. The FTJ area was reduced from 42,000 to 255 nm<sup>2</sup>, and the scaling behavior of the TER effect in 3 nm-thick YHO<sub>7</sub> devices closely resemble that in 2 nm-thick devices. The OFF-state current decreased with a slope of 1.1 between 42,000 and 2,600 nm<sup>2</sup>, followed by a steeper reduction below 2,600 nm<sup>2</sup>, whereas the ON-state current decreased more gradually with a slope of 0.30. These contrasting area dependences are attributed to the suppression of leakage pathways along grain boundaries in the OFF state and uniformly aligned remanent polarization in a small number of grains in the ON state. The demonstrated nanocrossbar FTJs highlight a promising route toward high-density, energy-efficient, and CMOS-compatible integration of ferroelectric memory.

## Introduction

The rapid advancement of artificial intelligence (AI) and neuromorphic computing has increased the demand for memory devices that are not only non-volatile but also exhibit fast switching speeds, high scalability, compatibility with complementary metal-oxide semiconductor (CMOS) technology, and low power consumption—key attributes for integrating memory and computation in AI-driven systems.<sup>1–5</sup>

Ferroelectric materials have emerged as promising candidates for non-volatile memory applications owing to their electrically switchable spontaneous polarization.<sup>6–8</sup> Among the most investigated device architectures are ferroelectric field-effect transistors (Fe-FETs) and ferroelectric tunnel junctions (FTJs). The FTJ is a two-terminal, non-volatile memory element that enables fast switching, long endurance, non-destructive readout, and a high ON/OFF resistance ratio, making it well-suited for next-generation storage-class memory.<sup>8,9,10,11</sup> It typically consists of a metal/ferroelectric/metal heterostructure, in which the incomplete screening of polarization charges by the electrodes and the use of ultrathin ferroelectric barriers enable modulation of the tunneling barrier height and width through polarization switching.<sup>12–14</sup> This modulation results in a change in tunneling resistance between low-resistance (ON) and high-resistance (OFF) states, a phenomenon known as the tunneling electroresistance (TER) effect.<sup>15</sup>

Esaki et al. first proposed the FTJ concept in 1971.<sup>16</sup> Realization of FTJs requires ultrathin ferroelectric barriers that support direct tunneling. However, as the ferroelectric layer thickness is scaled down to the nanometer regime, size effects arising from grain size, domain structure, lattice strain, and surface energy can degrade or suppress ferroelectricity.<sup>17,18</sup> When combined with depolarization fields, the size effects often lead to a critical thickness below which ferroelectricity is lost.<sup>19,20</sup> Contreras et al. reported early FTJ behavior in a 6 nm-thick PbZr<sub>0.52</sub>Ti<sub>0.48</sub>O<sub>3</sub> film sandwiched between SrRuO<sub>3</sub> and Pt electrodes,<sup>21</sup> marking the beginning of substantial FTJ research based on perovskite ferroelectrics.<sup>22,23,24</sup> However, perovskite-based FTJs face challenges such as size-dependent ferroelectric degradation, high crystallization temperatures, and poor CMOS compatibility.<sup>24</sup>

Hafnium oxide (HfO<sub>2</sub>) has emerged as a high- $\kappa$  dielectric widely adopted in industry as a gate insulator, offering superior compatibility with CMOS platforms.<sup>25</sup> In 2011, Börske et al. discovered that Si-doped HfO<sub>2</sub> exhibits ferroelectric behavior, paving the way for doped-HfO<sub>2</sub>-based ferroelectric thin films.<sup>26</sup> Ferroelectricity in HfO<sub>2</sub> is associated with the non-centrosymmetric orthorhombic phase (Pca2<sub>1</sub>), which can be

<sup>a</sup> Materials and Structures Laboratory, Institute of Integrated Research, Institute of Science Tokyo, Yokohama, 226-8503, Japan E-mail: majima@mml.titech.ac.jp

<sup>b</sup> School of Materials and Chemical Technology, Institute of Science Tokyo, Yokohama, 226-8503, Japan

<sup>†</sup> Electronic supplementary information (ESI) available.

See DOI: 10.1039/x0xx00000x



stabilized through chemical doping, interface engineering, or thermal treatment.<sup>26–29</sup> Unlike perovskite ferroelectrics, HfO<sub>2</sub>-based ferroelectrics exhibit mitigated size effects, owing to their fluorite-derived structure that reduces lattice distortions and surface-related instabilities at single nanoscale thickness.<sup>30</sup> These features, combined with a high dielectric constant, make doped-HfO<sub>2</sub> a strong candidate for use as a tunneling barrier in FTJs.

We recently reported that Y<sub>2</sub>O<sub>3</sub> is a promising dopant for HfO<sub>2</sub> due to its low sensitivity to surface energy, a feature not commonly observed in other doped-HfO<sub>2</sub> systems.<sup>31</sup> Stable remanent polarization was confirmed in nanometer-thick Y<sub>2</sub>O<sub>3</sub>-doped HfO<sub>2</sub> films grown directly on Pt/Ti/SiO<sub>2</sub>/Si substrates. Furthermore, we demonstrated the room-temperature growth of polycrystalline 7% Y-doped HfO<sub>2</sub> (YHO<sub>7</sub>) by RF magnetron sputtering, which exhibits clear ferroelectric behavior.<sup>32</sup> These results highlight YHO<sub>7</sub> as a viable candidate for tunneling barriers in FTJ applications.

TER effects have been demonstrated at lateral dimensions below 100 nm, aligning with the requirements for high-density FTJ memory integration.<sup>33–36</sup> For instance, conductive atomic force microscopy (c-AFM) studies have shown TER ratios

exceeding 10<sup>3</sup> in perovskite FTJs.<sup>33–35</sup> Abuwasib et al. employed hydrogen silsesquioxane (HSQ) planarization to fabricate perovskite-based FTJs with a TER ratio of 125.<sup>34</sup>

Recently, we demonstrated robust Pt nanogap electrodes with 10 nm linewidths by electron-beam lithography (EBL)<sup>37</sup> and achieved in-plane ferroelectric memory operation in 100 nm channel-length  $\alpha$ -In<sub>2</sub>Se<sub>3</sub> devices on SiO<sub>2</sub>/Si substrates.<sup>38</sup> For practical high-density memory integration, FTJ fabrication directly on SiO<sub>2</sub>/Si substrates via streamlined processes is highly desirable. The crossbar structure provides a compact and regular array format that facilitates two-terminal addressing and high cell density, making it particularly suitable for scalable ferroelectric memory architectures.

In this study, we demonstrate scalable nanocrossbar FTJs fabricated by a double-exposure EBL process. The devices consist of Ti/TiO<sub>x</sub> electrode/YHO<sub>7</sub> (2 and 3 nm)/Pt stacks on thermally oxidized Si substrates, with lateral dimensions down to 25 nm. The temperature dependence of the TER effect at 9 and 300 K confirms tunneling conduction in both the low- and high-resistance states. A maximum TER ratio of  $2.2 \times 10^3$  is achieved in a 3 nm YHO<sub>7</sub> nanocrossbar FTJ with an effective area of  $26 \times 24 \text{ nm}^2$ , and the area scaling of the TER effect is

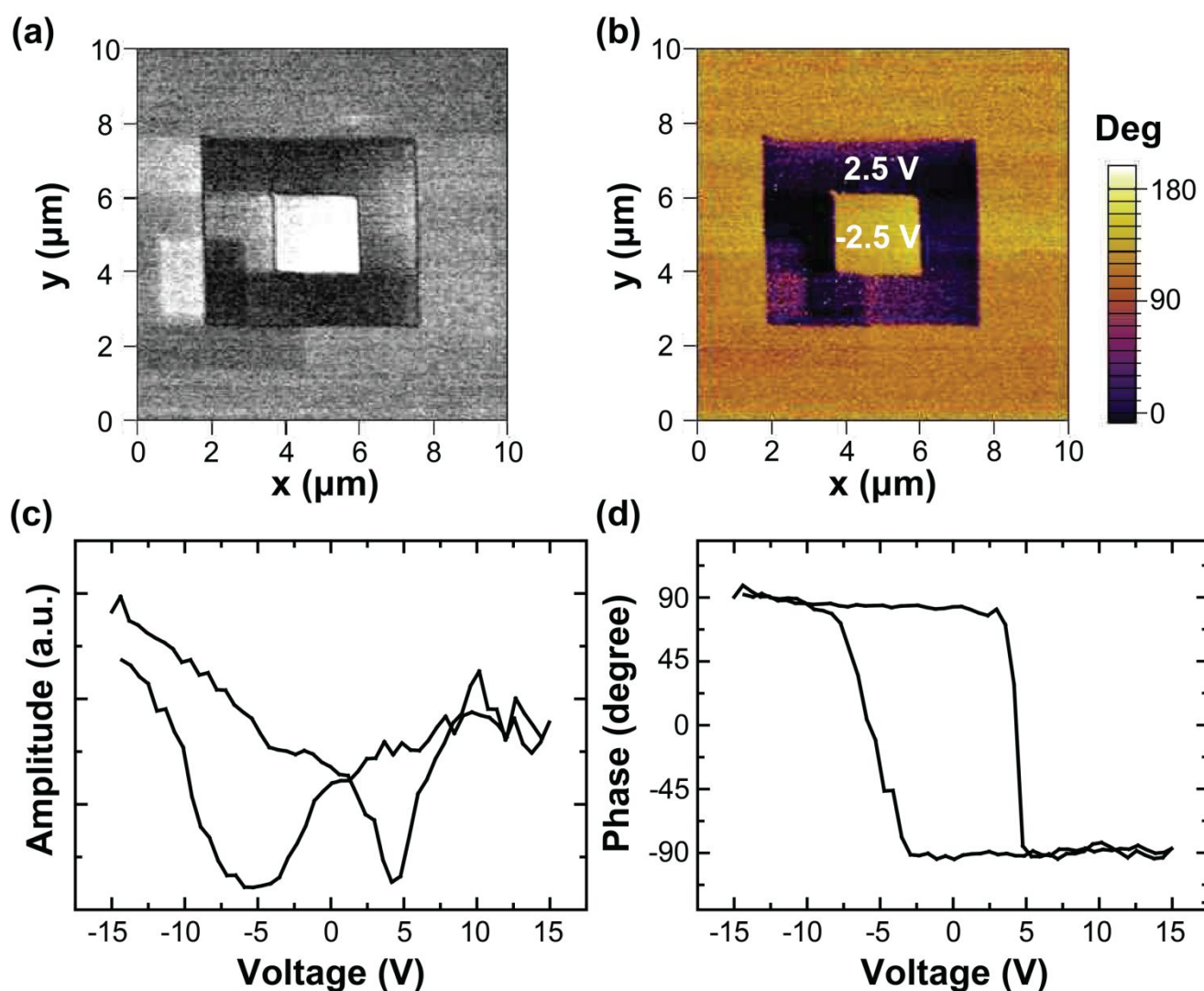


**Figure 1.** Local PFM box-in-box a) amplitude, and b) phase contrast images and PFM c) amplitude, and d) phase hysteresis loops of 3 nm-thick YHO<sub>7</sub> film on a Pt/Ti/SiO<sub>2</sub>/Si substrate.

x



systematically investigated. These results highlight the promise of nanocrossbar FTJs for high-density, energy-efficient, and CMOS-compatible, scalable integration of ferroelectric memory.

## Results and discussion

### Characterization of ferroelectricity of YHO<sub>7</sub>

The ferroelectric properties of an ultrathin YHO<sub>7</sub> film, suitable for enabling direct tunneling, were investigated using piezoresponse force microscopy (PFM).<sup>39</sup> A 3 nm YHO<sub>7</sub> film was deposited on a Pt/Ti/SiO<sub>2</sub>/Si substrate by radio-frequency magnetron sputtering at room temperature. The local PFM amplitude and phase contrast images, as well as the film's hysteresis loops, are shown in **Figure 1**.

A -2.5V pulse was first applied at the outer square (6 × 6 μm), and, subsequently, a 2.5 V pulse was applied at the inner square (2 × 2 μm<sup>2</sup>). Box-in-box PFM amplitude and phase contrast images are shown in **Figure 1a** and **1b**, respectively.

A butterfly-shaped amplitude loop and a phase hysteresis loop with 180° shift were observed (**Figures 1c** and **1d**), confirming ferroelectric switching behavior in 3 nm-thick YHO<sub>7</sub>. It notes that the 3 nm YHO<sub>7</sub> film exhibited clear amplitude and phase hysteresis loops from the first cycle of voltage sweep,

### Fabrication of scalable nanocrossbar FTJs

View Article Online

DOI: 10.1039/D5NR04010H

Straightforward fabrication processes were developed to prepare 25 nm square nanocrossbar Ti/TiO<sub>x</sub>/YHO<sub>7</sub>/Pt FTJs using double-exposure EBL on SiO<sub>2</sub>/Si substrates. A top-view SEM image of the 25 nm-square nanocrossbar Ti/TiO<sub>x</sub>/YHO<sub>7</sub>/Pt FTJs is shown in **Figure 2a**. In this nanocrossbar FTJ, the bottom Pt and top Ti/TiO<sub>x</sub> electrode widths are 26 nm and 24 nm, respectively, yielding an effective junction area of 624 nm<sup>2</sup>.

**Figure 2b** shows a cross-sectional SEM image of the Ti/TiO<sub>x</sub>/YHO<sub>7</sub>/Pt structure with false coloring applied to the Ti/TiO<sub>x</sub> (blue), YHO<sub>7</sub> (light ochre), and Pt (purple) layers. The bottom Pt nanowire electrode, composed of Pt (6 nm)/Ti (1 nm adhesion layer), was prepared by EBL, and then annealed in 3% H<sub>2</sub>/Ar at 550 °C for 5 min. The cross-sectional shape of the bottom Pt nanowire electrode transformed from rectangular to a semicircular arch, as shown in the cross-sectional SEM image in **Figure 2b**. During this annealing process, the Pt crystallinity improved.<sup>40,41</sup>

YHO<sub>7</sub> films with thicknesses of 2 and 3 nm were subsequently deposited by RF magnetron sputtering onto the curved bottom Pt nanowire electrodes.<sup>32</sup> As observed in **Figure 2b**, the semicircular Pt geometry facilitates conformal deposition of ultrathin YHO<sub>7</sub> films, supporting the formation of FTJ structure without short-circuiting. The top Ti nanowire

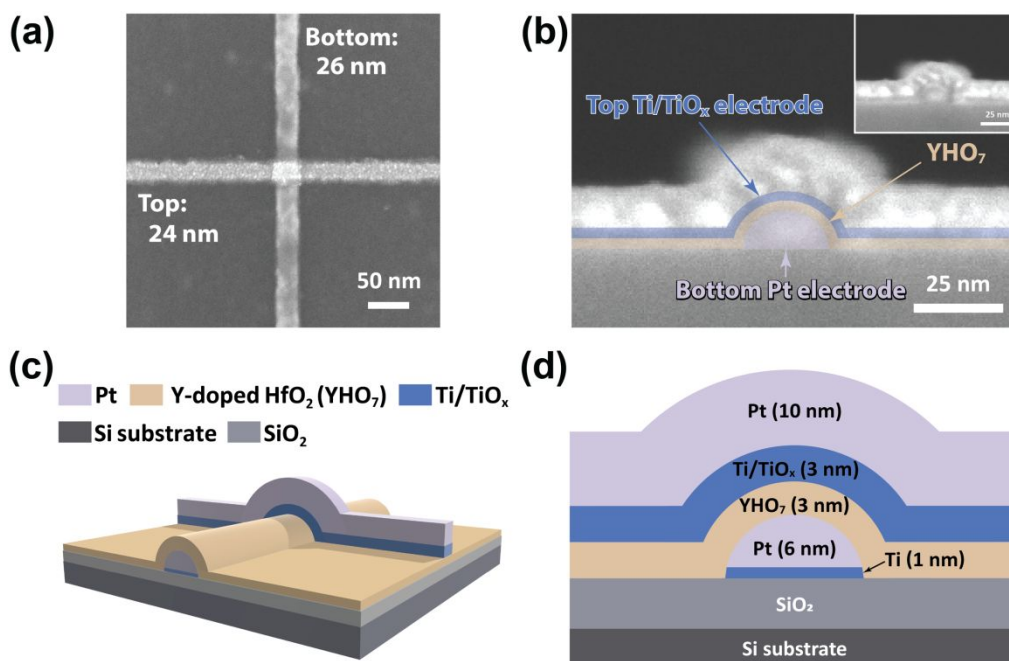


**Figure 2.** a) Top-view SEM image of a nanocrossbar Ti/TiO<sub>x</sub>/YHO<sub>7</sub> (3 nm)/Pt ferroelectric tunnel junction (FTJ) with an area of 624 nm<sup>2</sup> (26 × 24 nm). b) Cross-sectional SEM image of the Ti/YHO<sub>7</sub>/Pt structure with false coloring to highlight the Ti/TiO<sub>x</sub> (blue), YHO<sub>7</sub> (light ochre), and Pt (purple) layers. The original image is shown at the top-right inset. For this cross-sectional view, the top Ti and Pt electrodes are successively deposited as continuous films rather than as nanowires. c) 3D schematic and d) cross-sectional schematics of the nanocrossbar Ti/TiO<sub>x</sub>/YHO<sub>7</sub>/Pt FTJ.

indicating the presence of stable spontaneous polarization in the as-deposited state.

electrode, consisting of Pt (10 nm)/Ti (3 nm), was prepared by overlay EBL.





**Figure S1** shows a cross-sectional bright-field TEM (BF-TEM) image, and **Figure S2** presents the corresponding EDS elemental mapping (Supporting Information). The cross-sectional TEM image is consistent with the FE-SEM image in Figure 2b, and the EDS elemental mapping confirms that the layer sequence corresponds to a Ti/TiO<sub>x</sub>/YHO<sub>7</sub>/Pt stack structure with false coloring in Figure 2b.

Consequently, three-dimensional and cross-sectional schematic illustrations of the nanocrossbar Ti/TiO<sub>x</sub>/YHO<sub>7</sub>/Pt FTJ structure are shown in **Figures 2c** and **2d**, respectively. The nanocrossbar FTJ consists of a YHO<sub>7</sub> layer sandwiched between a bottom semicircular Pt nanowire and a top Ti nanowire electrode.

#### TER effect of nanocrossbar FTJs

Current (*I*)-voltage (*V*) hysteresis loops of a 3 nm-thick YHO<sub>7</sub> nanocrossbar FTJ with an area of 896 nm<sup>2</sup> (32 × 28 nm) were measured at room temperature (300 K) and 9 K (**Figure 3a**). Typical *I*-*V* characteristics loops of 3 and 2-nm thick YHO<sub>7</sub> nanocrossbar FTJs between 255 and 42,000 nm<sup>2</sup> at room temperature are shown in **Figures S3** and **S4**, respectively (Supporting Information).

It is noted that the shape and the current values of the *I*-*V*

hysteresis loop at 300 K are almost the same as those at 9 K. When switching from OFF to ON at a positive voltage, the transition occurred abruptly. In contrast, the ON-to-OFF transition occurred gradually with increasing negative applied voltage. The coercive voltages from the OFF-to-ON transition were 1.6 and 1.8 V at 300 and 9 K, respectively, and those from the ON-to-OFF gradual transition were -1.0 to -1.3 V (300 K) and -1.2 to -1.8 V (9 K). The magnified *I*-*V* characteristics in the ON and OFF states are shown in the inset of Figure 3a, where the current was approximately proportional to the voltage at 300 and 9 K. As the ON and OFF currents at 9 K are practically equal to those at 300 K and are proportional to voltage, the FTJ operation utilizes direct tunneling, which is highly dependent on the polarization direction.<sup>13</sup>

To further clarify the conduction mechanism, we analyzed the *I*-*V* characteristics of both the ON and OFF states in the intermediate voltage region ( $V < \varphi/e$ ), where  $\varphi$  is the tunneling barrier height and  $e$  is the elementary charge, using the Simmons direct tunneling model.<sup>42</sup> As shown in **Figure S5**, the theoretical curves calculated using the Simmons equation are in excellent agreement with the experimental data for both resistance states. The fitting parameters were  $\varphi = 1.7$  eV,  $d = 3.00$  nm, and  $m^* = 0.3 m_0$  for the low-resistance state

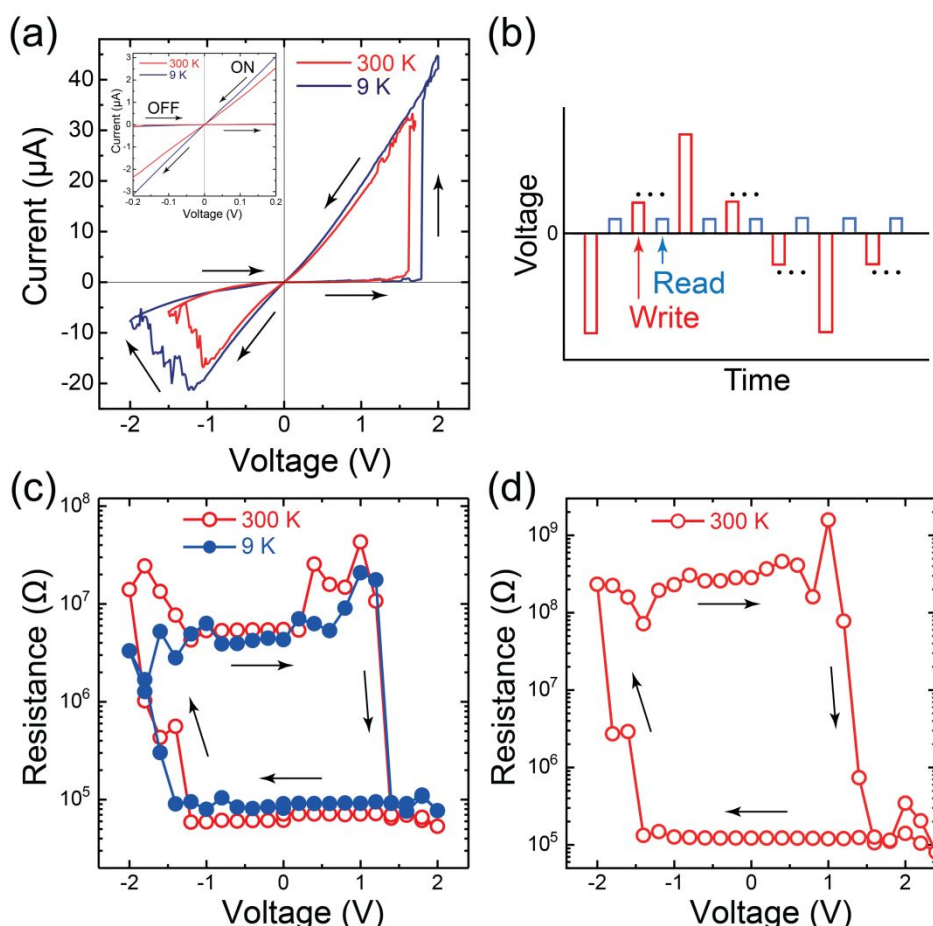


**Figure 3.** Switching behaviors of 3 nm-thick YHO<sub>7</sub> nanocrossbar FTJs. a) Temperature dependence of *I*-*V* hysteresis loops with almost 30 nm squared (896 nm<sup>2</sup>) at 300 K (red solid line) and 9 K (blue solid line). The magnified *I*-*V* characteristics under ON and OFF states (top left inset). b) The pulse sequence for *R*-*V* hysteresis loop. The write and read voltage widths are 200 ms and the read voltage was 0.1 V. c) Temperature dependence of *R*-*V* hysteresis loops at 300 K (red open circle) and 9 K (blue closed circle) on the FTJ in Figure 3a (30 nm squared). d) *R*-*V* hysteresis loop of 3 nm-thick YHO<sub>7</sub> nanocrossbar FTJ with 25 nm squared (624 nm<sup>2</sup>) at



(LRS), and  $\phi = 1.7$  eV,  $d = 3.48$  nm, and  $m^* = 0.3 m_0$  for the high-resistance state (HRS), where  $d$  is the tunneling barrier thickness,  $m^*$  is the electron effective mass, and  $m_0$  is the mass of electron. The identical barrier height and effective mass for both states, together with the small difference in effective barrier thickness of only 0.48 nm, indicate that the change in the depletion layer width at the  $\text{TiO}_x/\text{YHO}_7$  interface governs the resistance switching. These results unambiguously confirm that electron transport in both resistance states is dominated by direct tunneling through the ultrathin  $\text{YHO}_7$ -based ferroelectric barrier.

The resistance–voltage ( $R$ – $V$ ) hysteresis loops were measured using the pulse sequence illustrated in **Figure 3b**. **Figure 3c** shows the  $R$ – $V$  hysteresis loops of the same 3 nm-thick  $\text{YHO}_7$  nanocrossbar FTJ with  $896 \text{ nm}^2$  at 300 K and 9 K. This  $R$ – $V$  hysteresis loop of the FTJ displays well-defined memory characteristics. The  $R$ – $V$  hysteresis loop exhibits abrupt OFF-to-ON and gradual ON-to-OFF transition, which are consistent with the  $I$ – $V$  hysteresis loops. The coercive voltages for the OFF-to-ON transition are 1.2 V at both 300 and 9 K. In comparison, those for the ON-to-OFF transition are -1.2 V at 300 K and -1.4 V at 9 K. These results indicate that the OFF-to-ON switching is relatively insensitive to temperature. In contrast, the ON-to-OFF switching becomes slightly harder at lower temperatures.

The asymmetric resistive-switching behavior observed in the  $\text{Ti}/\text{TiO}_x/\text{YHO}_7/\text{Pt}$  nanocrossbar FTJ should arise from multiple interfacial and structural factors. First, the asymmetric electrode configuration produces different interface barrier heights due to the work-function difference between the  $\text{Ti}/\text{TiO}_x$  ( $\approx 4.3$  eV) and Pt ( $\approx 5.6$  eV) electrodes. This difference generates a built-in electric field across the junction, leading to asymmetric barrier modulation during switching.<sup>43,44,45</sup> Under positive bias (OFF-to-ON transition), the built-in field assists polarization reversal by lowering the effective tunneling barrier at the  $\text{Ti}/\text{TiO}_x$  interface, leading to a sharp increase in current. In contrast, under negative bias (ON-to-OFF transition), the field opposes polarization reversal, leading to a gradual decrease in current.

In addition to the work-function-induced barrier asymmetry, the nonplanar, curved surface geometry of the nanocrossbar FTJ further enhances the asymmetry. Because the  $\text{YHO}_7$  thin film conforms to the semicircular Pt nanowire electrode, strain gradients naturally develop along the film thickness, inducing flexoelectric polarization.<sup>46,47</sup> The resulting flexoelectric field modifies the local electric potential, facilitating polarization nucleation during the OFF-to-ON process and stabilizing residual polarization during the ON-to-OFF transition. Consequently, the observed asymmetric  $I$ – $V$  characteristics arise from the combined effects of the work-function-driven built-in field, the flexoelectric response associated with the curved device geometry, and local domain-wall pinning.

This combined mechanism is consistent with the experimentally observed sharp ON-switching transition and gradual OFF-switching decay. These findings provide a comprehensive physical picture that explains the bias-polarity-

dependent asymmetry in the tunneling characteristics of the nanocrossbar FTJ.

DOI: 10.1039/D5NR04010H

In **Figure 3c**, the resistance values of the LRS and HRS are  $7.8 \times 10^4 \Omega$  and  $5.5 \times 10^6 \Omega$  at 300 K, and  $8.9 \times 10^4 \Omega$  and  $4.3 \times 10^6 \Omega$  at 9 K, respectively. The corresponding TER ratios of the 3 nm-thick  $\text{YHO}_7$  nanocrossbar FTJ with  $896 \text{ nm}^2$  at 300 K and 9 K are 71 and 48, respectively. It notes that the resistance ratios between 300 K and 9 K under LRS and HRS are 1.1 and 0.8, respectively, indicating minimal change in resistance despite the significant temperature difference, suggesting that transport is dominated by tunneling conduction with only a minor contribution from thermally activated processes. Compared with previously reported  $\text{BaTiO}_3$ - or  $\text{HfO}_2$ -based FTJs, where the OFF-state resistance generally shows a stronger temperature dependence due to trap-assisted or thermionic conduction,<sup>13</sup> the present  $\text{YHO}_7$  nanocrossbar FTJ exhibits a remarkably weaker temperature dependence, highlighting the advantage of stabilized tunneling transport in this nanocrossbar FTJ.

**Figure 3d** shows an  $R$ – $V$  hysteresis loop of a 3 nm-thick  $\text{YHO}_7$  nanocrossbar FTJ with 25 nm squared ( $624 \text{ nm}^2$ ) at 300 K. The  $R$ – $V$  hysteresis loop exhibits well-defined memory characteristics. The resistances of LRS and HRS are  $8.9 \times 10^4 \Omega$  and  $4.3 \times 10^6 \Omega$ , respectively, yielding a TER ratio of  $2.2 \times 10^3$ . This TER ratio of  $2.2 \times 10^3$  is more than one order of magnitude higher than that of the 30-nm crossbar device (TER = 71 at 300 K) in **Figure 3c**, indicating that device scaling substantially enhances the tunneling electroresistance effect. In the present 25 nm squared nanocrossbar FTJ, the transports under LRS and HRS are clearly dominated by direct tunneling conduction, as evidenced by the extremely weak temperature dependence of both LRS and HRS. While thermally activated processes significantly contributed to HRS in previous reports.<sup>13,35,36,48,49</sup>

As observed in the  $R$ – $V$  hysteresis loops in **Figure 3c** and **3d**, resistance gradually increases from ON to OFF and resistance abruptly decreases from OFF to ON, aligning well with the  $I$ – $V$  hysteresis loops as shown in **Figure 3a**.

The coercive voltages at 300 K are evaluated as -1.4 V from ON-to-OFF and 1.0 V from OFF-to-ON from  $R$ – $V$  hysteresis loop in **Figure 3d**, which agrees with the coercive voltages of **Figure 3c** (-1.2 and 1.0 V, respectively). The average coercive electric field is calculated to be 4.0 MV/cm (1.2 V across 3 nm), which is in good agreement with our previous report ( $\sim 4.3$  MV/cm).<sup>50,51</sup>

The coercive voltages at 9 K are also evaluated as -1.4 V from ON to OFF and 1.2 V from OFF to ON, as indicated by the  $R$ – $V$  hysteresis loop in **Figure 3c**. These small temperature dependencies of the coercive voltages of the ON and OFF states at 300 K and 9 K agree well with the stable ferroelectricity and coercivity of the wake-up-free  $\text{Hf}_{0.5}\text{Zr}_{0.5}\text{O}_2$  thin film over a wide temperature range from room temperature (300 K) to cryogenic temperature (30 K).<sup>52</sup> The temperature independence of resistance states also proves the TER effect on the 3 nm-thick  $\text{YHO}_7$  nanocrossbar FTJ based on polarization switching.

**Figures 4a** and **4b** show the band diagrams of the ON (LRS) and OFF (HRS) states of the nanocrossbar FTJ with a junction



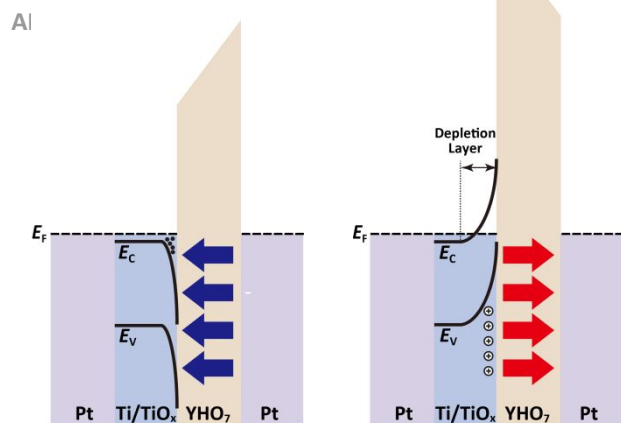


**Figure 4.** Energy band diagrams of FTJs in a) ON (LRS), and b) OFF (HRS) states. In LRS state (a), the polarization is pointing to Ti/TiO<sub>x</sub> side, and accumulates electrons at the TiO<sub>x</sub> surface. In HRS state (b), the polarization is pointing to Pt side, and deplete electrons at the TiO<sub>x</sub> surface, which make the effective tunnel barrier width increase.

structure of Ti/TiO<sub>x</sub> (top electrode)/YHO<sub>7</sub>/Pt (bottom electrode) structure under opposite spontaneous polarization directions of YHO<sub>7</sub>, respectively. At the Ti/YHO<sub>7</sub> interface, Ti scavenges oxygen from YHO<sub>7</sub>, and Ti is partially oxidized at the interface, forming a Ti/TiO<sub>x</sub>/YHO<sub>7</sub> structure at room temperature.<sup>53,54,55</sup> M. Sowinska et al. reported a TiO<sub>x</sub> thickness of 1.3 nm at the Ti/HfO<sub>2</sub> interface based on x-ray reflection (XRR) and scanning transmission electron microscopy (STEM) with energy-dispersive x-ray spectroscopy (EDX) measurements.<sup>53</sup> The spontaneous polarization induces bound charges at the interfaces of the YHO<sub>7</sub> thin film, which are compensated at the top Ti/TiO<sub>x</sub> and bottom Pt electrodes. In Pt, the screening effect is essentially polarity-independent owing to the large, nearly symmetric density of states near the Fermi level. In contrast, as TiO<sub>x</sub> is an *n*-type semiconductor, when the polarization is pointing to the Ti/TiO<sub>x</sub> side (Figure 4(a)), electrons accumulate at the TiO<sub>x</sub> surface. Then, the effective barrier height decreases, and the direct tunneling barrier width becomes the thickness of YHO<sub>7</sub>, resulting in LRS. On the other hand, when the polarization is pointing to the Pt side, positive charges are induced at the TiO<sub>x</sub>/YHO<sub>7</sub> interface and electrons are depleted at the TiO<sub>x</sub> surface. This results in both the effective tunnel barrier height and tunneling distance increasing owing to the depletion layer (HRS).

Compared with conventional metal/HfO<sub>2</sub>-based ferroelectric/SiO<sub>x</sub>/Si structures,<sup>48</sup> the Ti/TiO<sub>x</sub>/YHO<sub>7</sub>/Pt junction exhibits several advantages. First, the metal/ferroelectric/metal configuration eliminates the need for a SiO<sub>x</sub> interlayer, which can lead to interface charge. Second, the polarity-dependent interfacial response at the TiO<sub>x</sub>/YHO<sub>7</sub> contact enables a well-defined modulation of the tunneling barrier, resulting in a large ON/OFF ratio, as shown in Figure 3. YHO<sub>7</sub> with high crystallinity can be directly grown on the Pt surface by sputtering at room temperature, thereby suppressing leakage paths that are often present in HfO<sub>2</sub>/SiO<sub>x</sub>/Si devices. Finally, the CMOS-compatible YHO<sub>7</sub> and scalable metal/ferroelectric/metal geometry make the

TiO<sub>x</sub>/YHO<sub>7</sub>/Pt structure a promising platform for high-density non-volatile memories.

DOI: 10.1039/D5NR04010H

The abrupt decrease in resistance from the OFF to ON state and the gradual increase in resistance from the ON to OFF state in the *R-V* and *I-V* results (Figure 3) arise from distinct polarization-switching processes.<sup>56</sup> During the ON to OFF transition, domain-wall pinning provides pre-existing nucleation sites, facilitating gradual polarization reversal under an increasing electric field. In contrast, the OFF-to-ON transition requires the activation of new nucleation centers, leading to an abrupt polarization-switching event. Such asymmetric switching behavior is consistent with previous reports of defect-mediated pinning in HfO<sub>2</sub>-based FTJs, in which oxygen vacancies and hydrogen-related complexes hinder polarization reversal until passivation treatments are applied.<sup>57</sup> Interface-induced pinning due to oxygen-vacancy segregation and electrode scavenging has also been shown to significantly affect the TER.<sup>58</sup> In addition, direct spectroscopic evidence of domain-wall pinning in ferroelectric HfO<sub>2</sub> thin films supports our interpretation that domain-wall pinning acts as a nucleation source during gradual ON to OFF switching.<sup>59</sup>

It noted that these asymmetrical resistance-switching behaviors were observed in the nanocrossbar FTJ area of 896 nm<sup>2</sup>. The gradual resistance transition from the ON to OFF state suggests a self-polarization reversal with a gradual domain growth process even in the small FTJ area of 896 nm<sup>2</sup>. An abrupt transition from OFF to ON in resistance suggests simultaneous self-polarization switching across all domains within the crossbar FTJ at 896 nm<sup>2</sup>. This nanocrossbar FTJ opens up possibilities for advanced multi-state memory applications, leveraging domain-forming mechanisms and asymmetrical resistance-switching behavior in small FTJ areas.

#### Nanocrossbar FTJ area dependence on the TER effect

The nanocrossbar FTJ area dependence on the ON current (*I*<sub>ON</sub>), OFF current (*I*<sub>OFF</sub>), and TER ratio is shown in Figure 5 for nanocrossbar FTJ with YHO<sub>7</sub> thicknesses of 2 and 3 nm. The read currents were measured at 0.1 V. Both *I*<sub>OFF</sub> and *I*<sub>ON</sub> decreased with decreasing nanocrossbar FTJ area from 42,000 nm<sup>2</sup> to 255 nm<sup>2</sup> (2nm-thick YHO<sub>7</sub>) and 624 nm<sup>2</sup> (3nm-thick YHO<sub>7</sub>). The *I*<sub>OFF</sub> and *I*<sub>ON</sub> slopes relative to the FTJ area are calculated as shown in Figure 5.

For *I*<sub>OFF</sub> of nanocrossbar FTJs, the slopes with the reduction of FTJ area are 1.0 (black dotted line) and 1.1 (black solid line) between 42,000 and 1,476 nm<sup>2</sup> (2 nm-thick YHO<sub>7</sub>), and between 41,370 and 2,597 nm<sup>2</sup> (3 nm-thick YHO<sub>7</sub>), respectively. It noted those *I*<sub>OFF</sub> slopes values of approximately 1 follow Ohm's law, in which the resistance is inversely proportional to the area. When the FTJ area is less than 1,476 nm<sup>2</sup> (2 nm-thick YHO<sub>7</sub>) and 2,597 (3 nm-thick YHO<sub>7</sub>), *I*<sub>OFF</sub> decreases more rapidly with area, and the slopes are 2.4 and 3.0 between 1,476 and 255 nm<sup>2</sup>, and between 2,597 and 624 nm<sup>2</sup>, respectively.

To examine the device-to-device consistency, several nanocrossbar Ti/TiO<sub>x</sub>/YHO<sub>7</sub>/Pt FTJs with identical lateral dimensions of 50 × 50 nm<sup>2</sup> were characterized and summarized in Supporting Information (Figure S6). *I*<sub>ON</sub> and *I*<sub>OFF</sub>,



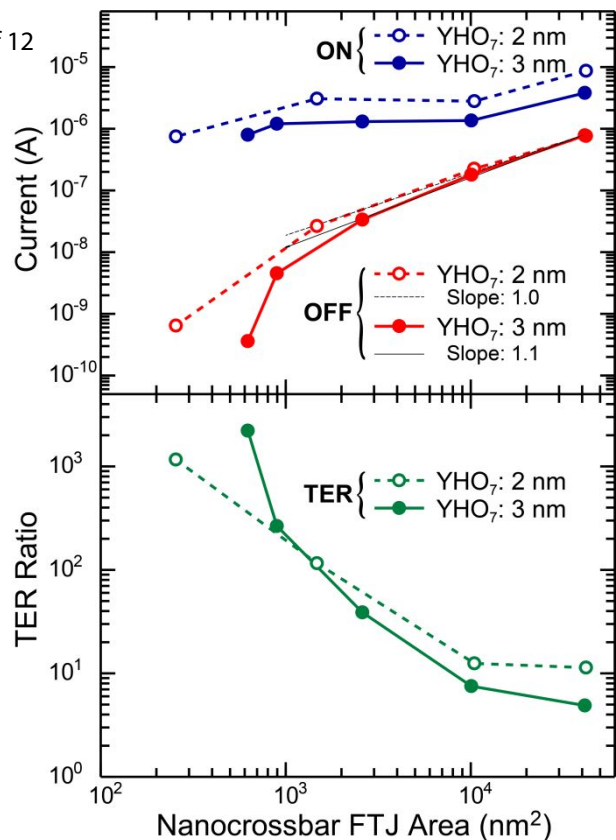


**Figure 5.** Nanocrossbar FTJ area dependence of  $I_{ON}$ ,  $I_{OFF}$  (upper), and TER ratio (lower) on 2 nm and 3 nm-thick YHO<sub>7</sub>. Read voltage was 0.1 V.

as well as the resulting TER ratios, were found to be nearly identical among all measured devices, indicating good reproducibility and uniformity of the switching behavior. These results suggest that uniform ferroelectric switching behavior is maintained even in 3 nm-thick YHO<sub>7</sub> films where multiple structural phases may coexist.

McKenna et al. reported grain boundary-mediated leakage current in polycrystalline 5 nm HfO<sub>2</sub> thin films grown on *p*-type Si with a 1 nm-thick native SiO<sub>2</sub> layer, using conductive atomic force microscopy with a 6.5 V conductive tip voltage (resulting in *p*-type Si depletion).<sup>61</sup> It was concluded that the tunneling barrier is lowered at grain boundaries as a result of their intrinsic electronic properties and that leakage current tends to dominate grain boundaries.<sup>61</sup> The grain boundary length should be proportional to the FTJ area. When the grain size is smaller than the FTJ area, leakage paths at the grain boundary should be proportional to the FTJ area. The more rapid decreasing  $I_{OFF}$  compared with the theoretical change with decreasing YHO<sub>7</sub> nanocrossbar FTJ area should be attributed to the reduced defect-induced leakage paths, such as grain-boundary-induced leakage paths with a reduced FTJ area when minimizing FTJ size smaller than 2,500 nm<sup>2</sup>.<sup>61</sup>

This interpretation is corroborated by microscopic structural analysis. Cross-sectional BF-TEM and EDS elemental mapping (Figures S1 and S2) reveal that the 2–3 nm-thick YHO<sub>7</sub> film is conformally grown on the semicircular Pt nanowire electrode and does not exhibit extended columnar grains. High-resolution TEM further confirms that the smallest nanocrossbar junctions (25 nm in width) correspond to a single-grain or partially single-grain region of YHO<sub>7</sub>. Therefore, continuous grain-boundary networks capable of forming

leakage paths are absent at this scale, consistent with the rapid suppression of  $I_{OFF}$  in the smallest devices.

For  $I_{ON}$  of nanocrossbar FTJs, the slopes were 0.41 (2 nm-thick YHO<sub>7</sub>) and 0.30 (3 nm-thick YHO<sub>7</sub>) in the range of FTJ area between 42,000 and 255 nm<sup>2</sup> and between 41,370 and 624 nm<sup>2</sup>, respectively. These sub-linear slopes ( $< 1$ ) of  $I_{ON}$  indicate that the effective fraction of the active direct tunneling region for  $I_{ON}$  increases as the FTJ area decreases, reflecting the enhancement of the curved nanocrossbar geometry on the direct-tunneling area.

Boyn et al. reported that the ratio of effective switching domain area to FTJ area increases as the BiFeO<sub>3</sub> area is reduced from 1.13 μm<sup>2</sup> to 25,400 nm<sup>2</sup>, leading to improved uniformity of remanent polarization.<sup>62</sup> With decreasing FTJ area, the number of activated nucleation centers to turn the FTJ from the OFF state to the ON state should become small, and electrons at the Ti/TiO<sub>x</sub> interface should more uniformly accumulate at the whole nanocrossbar FTJ area. As a result, with the decreasing FTJ area,  $I_{ON}$  did not decrease below the theoretical slope of 1 due to more uniform domain switching.<sup>62</sup>

In Figure 5, nanocrossbar FTJ with 2 nm-thick YHO<sub>7</sub>, with decreasing FTJ area from 42,000 to 255 nm<sup>2</sup>,  $I_{ON}$  decreases from 8.7 μA to 0.75 μA, and  $I_{OFF}$  decreases from 0.77 μA to 0.63 nA, respectively, resulting in an elevation of the TER ratio from 11 to 1.2 × 10<sup>3</sup>. For a 3 nm-thick YHO<sub>7</sub> nanocrossbar FTJ, with decreasing FTJ area from 41,270 to 624 nm<sup>2</sup>,  $I_{ON}$  decreases from 3.8 μA to 0.80 μA, and  $I_{OFF}$  decreases from 0.78 μA to 0.36 nA, respectively, resulting in an elevation of the TER ratio from 4.9 to 2.2 × 10<sup>3</sup>. It noted that the ideal nanocrossbar FTJ area dependencies of  $I_{ON}$ ,  $I_{OFF}$ , and TER ratio have been observed in both YHO<sub>7</sub> thicknesses of 2 and 3 nm. Consequently, a TER ratio of 2.2 × 10<sup>3</sup> has been obtained on the nanocrossbar FTJ at the smallest area of 624 nm<sup>2</sup> on 3 nm-thick YHO<sub>7</sub> under the direct tunneling regime, even at HRS.



In most previously reported BaTiO<sub>3</sub>- and HfO<sub>2</sub>-based FTJs, the TER ratios at room temperature are typically in the range of 10–10<sup>3</sup>, which is comparable to the present nanocrossbar Ti/TiO<sub>x</sub>/YHO<sub>7</sub>/Pt FTJs exhibiting a TER of 2 × 10<sup>3</sup>. Although much higher TER ratios up to 10<sup>7</sup> have been reported for HfO<sub>2</sub>-based FTJs such as HZO/Nb (0.7 wt%)-doped SrTiO<sub>3</sub> (NSTO) heterojunctions, the huge resistance contrast in those systems primarily originates from the depletion region formed in the *n*-type NSTO semiconductor, which strongly suppresses the OFF-state current.<sup>10,49</sup> In our Ti/TiO<sub>x</sub>/YHO<sub>7</sub>/Pt nanocrossbar FTJs, a depletion layer may also form to some extent at the *n*-type TiO<sub>x</sub> interface; however, both the ON and OFF currents are governed by direct tunneling through the ultrathin YHO<sub>7</sub> barrier. This high-resistance-state tunneling behavior is supported by the observation that the ON- and OFF-state current levels and TER ratios remain nearly identical at 9 K and 300 K. Accordingly, the observed TER ratio of 2 × 10<sup>3</sup> represents a realistic value for intrinsic polarization-controlled tunneling in a metallic nanocrossbar FTJ, free from additional semiconductor depletion effects.

### Retention characteristics

Retention characteristic of 3 nm-thick YHO<sub>7</sub> nanocrossbar FTJs with 896 (32 × 28) nm<sup>2</sup> is shown in **Figure 6**. The ON and OFF states were measured using the pulse sequence illustrated in the insets. Initially, a negative erase pulse voltage of -2 V was applied to the bottom Pt electrode, switching the nanocrossbar FTJ to the high-resistance OFF state. Subsequent continuous read pulses of 0.1 V confirmed a stable OFF-state resistance of 2 × 10<sup>7</sup> Ω maintained for up to 1000 s. A positive write pulse voltage of 2 V was then applied, switching the nanocrossbar FTJ to the ON-state. A stable ON-state resistance of 2 × 10<sup>5</sup> Ω was retained for 1000 s. The resulting TER ratio of approximately 100 is consistent with the data presented in **Figure 3c**.

To further clarify the retention behavior, the same dataset shown in **Figure 6** was replotted as linear resistance (*R*)–log time graphs and is provided in **Figure S7** (Supporting Information). The ON-state current remained remarkably stable, showing almost no change over the entire measurement period (up to 10<sup>3</sup> s), whereas the OFF-state resistance gradually decreased with time. Extrapolation of the linear *R*–log time plot suggests that the OFF-state resistance, and consequently the TER ratio, would decrease to approximately half of its initial value after 10 years (≈ 3.15 × 10<sup>8</sup> s). Nevertheless, a clear contrast in resistance between the ON and OFF states would still be maintained.

The switching reliability of the nanocrossbar Ti/TiO<sub>x</sub>/YHO<sub>7</sub>/Pt FTJs was evaluated by endurance measurements using a device with a lateral dimension of 50 × 50 nm<sup>2</sup> and a 3 nm-thick YHO<sub>7</sub> layer (**Figure S3**). The device was repeatedly switched between the ON and OFF states by applying write and erase voltages of 2 V and -2 V, respectively, while the resistance was read at 0.1 V. The nanocrossbar FTJ exhibited stable and reproducible resistive switching without noticeable degradation, demonstrating that the device can withstand at

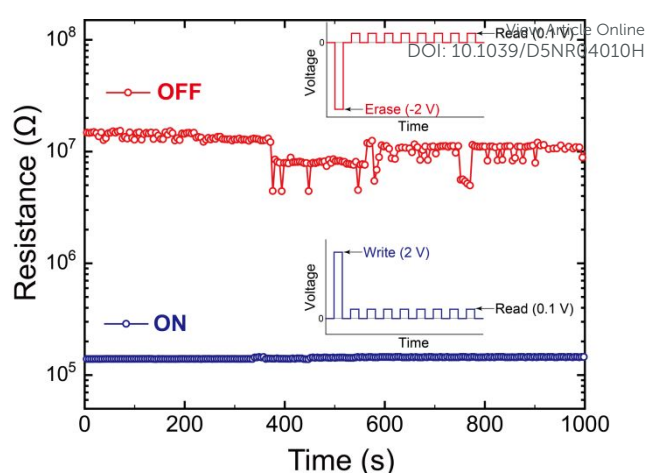


**Figure 6.** Retention characteristics of 3 nm-thick YHO<sub>7</sub> nanocrossbar FTJ with an area of 896 nm<sup>2</sup>, the pulse sequences are shown in the inset. The write, erase, and read voltages are 2, -2, and 0.1 V, respectively. All write, erase, and read pulse widths are 200 ms.

least 100 consecutive switching operations (**Figure S8**, Supporting Information). Those retention and endurance characteristics suggest robust long-term non-volatile functionality in nanocrossbar FTJ devices.

### Conclusions

We demonstrated scalable nanocrossbar-type FTJs using a double-exposure EBL process. Nanocrossbar FTJs consisting of top Ti/TiO<sub>x</sub> electrode/YHO<sub>7</sub>/bottom Pt electrode on SiO<sub>2</sub>/Si substrates were fabricated with lateral dimensions down to 25 nm. The temperature dependence of the TER effect at 9 and 300 K reveals direct tunneling conduction not only in LRS but also in HRS. TER ratio of 2.2 × 10<sup>3</sup> was achieved in the 3 nm-thick YHO<sub>7</sub> nanocrossbar FTJ with a lateral dimension of 25 nm. Nanocrossbar FTJ area dependence of the TER effect coincides well with 3 and 2 nm-thick YHO<sub>7</sub>. The OFF-state current decreased with a slope of 1.1 between 42,000 and 2,597 nm<sup>2</sup>, then the slope became steeper below 2,597 nm<sup>2</sup>. On the contrary, the ON-state current slowly reduced with a slope of 0.30. The large (>1.1) and small (0.30) slopes in the OFF and ON-state current nanocrossbar area dependence were discussed in terms of the suppression of leakage pathways along grain boundaries and uniformly aligned remanent polarization in a small number of grains. The nanocrossbar FTJ is significant for high-density, energy-efficient, and CMOS-compatible integration of scalable ferroelectric memory.

### Experimental methods

#### Scalable nanocrossbar FTJ fabrication

The bottom nanowire electrodes, made of Pt (6 nm)/Ti (1 nm), are fabricated using electron-beam lithography (ELS-7500EX, Elionix, Japan) and E-beam evaporation, followed by a lift-off



process. The linewidth of the Pt nanowires is designed using CAD software for EBL. The bottom Pt electrodes are then annealed in a 3% H<sub>2</sub>/Ar mixture for 5 min at 550 °C. As shown in the SEM image (Figure 2b), the cross-sectional shape of the bottom Pt electrode deformed from rectangular to a semicircular arch, known as Rayleigh instability, to reduce surface free energy and improve the crystallinity of the bottom Pt nanowire during the annealing.<sup>40,41</sup>

YHO<sub>7</sub> ultrathin films with thicknesses of 3 and 2 nm are deposited onto a bottom Pt/Ti nanowire and a SiO<sub>2</sub>/Si substrate using RF magnetron sputtering with a 2-inch diameter YHO<sub>7</sub> ceramic target (Toshiba Manufacturing, Japan).<sup>32</sup> The distance between the target surface and the substrate is 70 mm. Sputtering is carried out in a pure Ar ambient at a total pressure of 10 mTorr with an RF power of 50 W. No thermal treatment is applied to the YHO<sub>7</sub> thin film during sputtering or after deposition.

For the top Ti nanowire electrodes, Pt (10 nm)/Ti (3 nm) was deposited using a double-exposure EBL process followed by E-beam evaporation and a lift-off process. Uniform nanocrossbar Ti/TiO<sub>2</sub>/YHO<sub>7</sub>/Pt junctions are prepared as shown in the cross-sectional SEM image (Fig. 2(b)). Using a designed mask, the probing pads for the bottom and top Pt (40 nm)/Ti (5 nm) electrodes are fabricated by photolithography, E-beam evaporation, and a lift-off process.

#### Ferroelectric YHO<sub>7</sub> film characterizations

PFM measurement of ferroelectric 3 nm-thick YHO<sub>7</sub> thin film is characterized with an atomic force microscope (Asylum Research Cypher, Japan, MFP-3D scanning probe microscope) by using Pt/Ir-coated Si cantilever tips (NanoAndMore, USA, nominal spring constant 2.8 N/m). A bidirectional bias sweep between -15 V and 15 V is applied to measure hysteresis loops under Dual-Resonance Amplitude Tracking (DRAT) mode.<sup>39</sup>

#### Nanocrossbar FTJ switching properties measurements

Electrical properties of nanocrossbar FTJs were measured using a mechanical helium refrigerator multi-prober (GRAIL10-LOGOS01S, Nagase, Japan) and a semiconductor parameter device analyzer (B1500, Keysight, USA). FTJ switching property measurement temperature was 300 and 9 K. All measurements were conducted under a vacuum ( $\approx 10^{-4}$  Pa) and in a dark environment. The temperature dependence of the current-voltage (*I*-*V*) hysteresis loop was measured by applying a triangular voltage waveform to the bottom Pt electrode at 0.02 Hz. The TER ratio is calculated from the current-voltage characteristics, defined as  $(R_{\text{OFF}} - R_{\text{ON}})/R_{\text{ON}} \times 100\%$ , where  $R_{\text{OFF}}$  and  $R_{\text{ON}}$  are the FTJ resistances for the OFF and ON states, respectively, at a voltage of 0.1 V.

As shown in **Figure 3b**, the resistance-voltage (*R*-*V*) hysteresis loop was measured as follows: A negative write pulse of -2 V was first applied to the bottom Pt electrode, setting the junction to a high-resistance (OFF) state. Then, the read voltage was set to 0.1 V. Subsequently, positive voltage pulses were applied in steps from 0.2 V to 2 V (or 2.4 V) in 0.2 V increments. The voltage was then swept down from 2 (or 2.4) V to -2 V in -0.2 V steps, and finally increased back to 0 V. After each write pulse, a read pulse of 0.1 V was applied to

probe the resistance. Both write and read pulses had widths of 200 ms.

DOI: 10.1039/D5NR04010H

After measuring the electrical properties, the nanocrossbar FTJs were characterized by FE-SEM (Regulus 8230, Hitachi High-Tech, Japan).

#### Author contributions

Y. M. conceived the research. Z. S. performed most of the FTJ device preparations and the electrical measurements. Y. N., K. O., and H. F. helped in the YHO<sub>7</sub> sputtering. Z. S., S. I., H. F., and Y. M. analyzed and discussed the experimental data. Z. S. and Y. M. wrote the manuscript.

#### Conflicts of interest

There are no conflicts to declare.

#### Data availability

Detailed electrical characterization results are shown in the ESI†.

#### Acknowledgements

This study was partially supported by the MEXT Program: Data Creation and Utilization Type Material Research and Development (Grant No. JPMXP1122683430), JST CREST (Grant Number JPMJCR22B4). H. F. thanks the MEXT Initiative to Establish Next-generation Novel Integrated Circuits Centers (X-NICS) (Grant No. JPJ011438), JST-Adopting Sustainable Partnerships for Innovative Research Ecosystem (ASPIRE) (Grant No. JPMJAP2312), and the Japan Society for the Promotion of Science (JSPS) KAKENHI (Grant No. 22K18307). Z. S. thanks JST SPRING (J). We also thank Ms. M. Miyakawa and Ms. I. Shimada, Institute of Science Tokyo, for their technical support.

#### References

- 1 S. Yu, *Semiconductor Memory Devices and Circuits*, CRC Press, Boca Raton, 2022.
- 2 W. Banerjee, *Electronics (Basel)*, 2020, **9**, 1029.
- 3 T. Endoh, H. Koike, S. Ikeda, T. Hanyu and H. Ohno, *IEEE J Emerg Sel Top Circuits Syst*, 2016, **6**, 109–119.
- 4 B. Prasad, Y. Huang, R. V. Chopdekar, Z. Chen, J. Steffes, S. Das, Q. Li, M. Yang, C. Lin, T. Gosavi, D. E. Nikonov, Z. Q. Qiu, L. W. Martin, B. D. Huey, I. Young, J. Íñiguez, S. Manipatruni and R. Ramesh, *Advanced Materials*, 2020, **32**, 2001943.
- 5 S. Manipatruni, D. E. Nikonov and I. A. Young, *Nat Phys*, 2018, **14**, 338–343.
- 6 S. Manipatruni, D. E. Nikonov, C.-C. Lin, T. A. Gosavi, H. Liu, B. Prasad, Y.-L. Huang, E. Bonturim, R. Ramesh and I. A. Young, *Nature*, 2019, **565**, 35–42.
- 7 S. Oh, H. Hwang and I. K. Yoo, *APL Mater*, 2019, **7**, 091109.
- 8 N. A. Spaldin and R. Ramesh, *Nat Mater*, 2019, **18**, 203–212.



- 9 Z. Wang, H. Wu, G. W. Burr, C. S. Hwang, K. L. Wang, Q. Xia and J. J. Yang, *Nat Rev Mater*, 2020, **5**, 173–195.
- 10 S. H. Park, H. J. Lee, M. H. Park, J. Kim and H. W. Jang, *J. Phys. D: Appl. Phys.*, 2024, **57**, 253002.
- 11 M. H. Park, H. J. Kim, Y. J. Kim, Y. H. Lee, T. Moon, K. Do Kim, S. D. Hyun, F. Fengler, U. Schroeder and C. S. Hwang, *ACS Appl Mater Interfaces*, 2016, **8**, 15466–15475.
- 12 P. Maksymovych, S. Jesse, P. Yu, R. Ramesh, A. P. Baddorf and S. V. Kalinin, *Science*, 2009, **324**, 1421–1425.
- 13 J. Hwang, Y. Goh and S. Jeon, *Small*, 2024, **20**, 2305271.
- 14 S. H. Park, H. J. Lee, M. H. Park, J. Kim and H. W. Jang, *J. Phys D: Appl Phys*, 2024, **57**, 253002.
- 15 Z. Wen and D. Wu, *Advanced Materials*, 2020, **32**, 1904123.
- 16 L. Esaki, R. B. Laibowitz and P. J. Stiles, *IBM Tech. Discl. Bull.*, 1971, **13**, 2161.
- 17 H. Qiao, C. Wang, W. S. Choi, M. H. Park and Y. Kim, *Materials Science and Engineering: R: Reports*, 2021, **145**, 100622.
- 18 S. Li, J. A. Eastman, J. M. Vetrone, C. M. Foster, R. E. Newnham and L. E. Cross, *Jpn J Appl Phys*, 1997, **36**, 5169.
- 19 V. M. Fridkin, S. Ducharme, A. V. Bune, S. P. Palto, S. G. Yudin and L. M. Blinov, *Ferroelectrics*, 2000, **236**, 1–10.
- 20 A. Gruverman, D. Wu, H. Lu, Y. Wang, H. W. Jang, C. M. Folkman, M. Ye. Zhuravlev, D. Felker, M. Rzechowski, C.-B. Eom and E. Y. Tsymbal, *Nano Lett*, 2009, **9**, 3539–3543.
- 21 J. Rodríguez Contreras, H. Kohlstedt, U. Poppe, R. Waser, C. Buchal and N. A. Pertsev, *Appl. Phys. Lett.*, 2003, **83**, 4595–4597.
- 22 W. Xiao, X. Zheng, H. Hao, L. Kang, L. Zhang, and Z. Zeng, *NPJ Comput Mater*, 2023, **9**, 144.
- 23 Z. Wang, W. Zhao, A. Bouchenak-Khelladi, Y. Zhang, W. Lin, J.-O. Klein, D. Ravelosona and C. Chappert, *J Phys. D: Appl Phys*, 2013, **47**, 045001.
- 24 J. Müller, T. S. Böscke, D. Bräuhäus, U. Schröder, U. Böttger, J. Sundqvist, P. Kücher, T. Mikolajick and L. Frey, *Appl Phys Lett*, 2011, **99**, 112901.
- 25 G. D. Wilk, R. M. Wallace and J. M. Anthony, *J Appl Phys*, 2001, **89**, 5243–5275.
- 26 T. S. Böscke, J. Müller, D. Bräuhäus, U. Schröder and U. Böttger, *Appl Phys Lett*, 2011, **99**, 102903.
- 27 M. H. Park, Y. H. Lee, H. J. Kim, Y. J. Kim, T. Moon, K. Do Kim, J. Müller, A. Kersch, U. Schroeder, T. Mikolajick and C. S. Hwang, *Advanced Materials*, 2015, **27**, 1811–1831.
- 28 M. Dogan, N. Gong, T.-P. Ma and S. Ismail-Beigi, *Physical Chemistry Chemical Physics*, 2019, **21**, 12150–12162.
- 29 S. K. Lee and C. W. Bark, *Journal of the Korean Ceramic Society*, 2022, **59**, 25–43.
- 30 J. Müller, T. S. Böscke, U. Schröder, S. Mueller, D. Brauhäus, U. Böttger, L. Frey and T. Mikolajick, *Nano Lett.* 2012, **12**, 4318.
- 31 S. Shi, H. Xi, T. Cao, W. Lin, Z. Liu, J. Niu, D. Lan, C. Zhou, J. Cao, H. Su, T. Zhao, P. Yang, Y. Zhu, X. Yan, E. Y. Tsymbal, H. Tian and J. Chen, *Nat Commun*, 2023, **14**, 1780.
- 32 T. Mimura, T. Shimizu, H. Uchida and H. Funakubo, *Appl Phys Lett*, 2020, **116**, 062901.
- 33 Z. Wang, Z. Guan, H. Sun, Z. Luo, H. Zhao, H. Wang, Y. Yin and X. Li, *ACS Appl Mater Interfaces*, 2022, **14**, 24602–24609.
- 34 X. S. Gao, J. M. Liu, K. Au and J. Y. Dai, *Appl Phys Lett*, 2012, **101**, 142905.
- 35 A. Chanthbouala, A. Crassous, V. Garcia, K. Bouzehouane, S. Fusil, X. Moya, J. Allibe, B. Dlubak, J. Grollier, S. Xavier, C. Deranlot, A. Moshar, R. Proksch, N. D. Mathur, M. Bibes and A. Barthélémy, *Nat Nanotechnol*, 2012, **7**, 101–104.
- 36 M. Abuwasib, J.-W. Lee, H. Lee, C.-B. Eom, A. Gruverman and U. Singiseti, *J. Vac. Sci. Technol: B*, 2017, **35**, 021803.
- 37 Y. Y. Choi, T. Teranishi and Y. Majima, *Appl Phys Express*, 2019, **12**, 025002.
- 38 S. Miao, R. Nitta, S. Izawa and Y. Majima, *Adv Sci*, 2023, **10**, 2370198.
- 39 A. Gruverman, and A. Kholkin, *Rep Prog Phys*, 2006, **69**, 2443.
- 40 R. Toyama, S. Kawachi, J. Yamaura, T. Fujita, Y. Murakami, H. Hosono and Y. Majima, *Nanoscale Adv*, 2022, **4**, 5270–5280.
- 41 M. Zhao, R. Nitta, S. Izawa, J. Yamaura, and Y. Majima, *Adv. Funct. Mater.*, 2025, **35**, 2415971.
- 42 J. G. Simmons, *J. Appl. Phys.*, 1963, **34**, 1793.
- 43 E. Y. Tsymbal and H. Kohlstedt, *Science*, 2006, **313**, 181–183.
- 44 M. Y. Zhuravlev, R. F. Sabirianov, S. S. Jaswal, and E. Y. Tsymbal, *Phys. Rev. Lett.*, 2005, **94**, 246802.
- 45 V. Garcia, M. Bibes, L. Bocher, S. Valencia, F. Kronast, A. Crassous, X. Moya, S. Enouz-Vedrenne, A. Gloter, D. Imhoff, C. Deranlot, N. D. Mathur, S. Fusil, K. Bouzehouane, and A. Barthélémy, *Science*, 2010, **327**, 1106–1110.
- 46 G. Catalan, A. Lubk, A. H. G. Vlooswijk, E. Snoeck, C. Magen, A. Janssens, G. Rispens, G. Rijnders, D. H. A. Blank and B. Noheda, *Nat. Mater.*, 2011, **10**, 963–967.
- 47 J. Narvaez, S. Saremi, J. Hong, M. Stengel, and G. Catalan, *Phys. Rev. Lett.*, 2015, **115**, 037601.
- 48 K. Lee, J. Byun, K. Park, S. Kang, M. S. Song, J. Park, J. Lee, S. C. Chae, *Appl Mater Today*, 2022, **26**, 101308.
- 49 Z. Gao, W. Zhang, Q. Zhong, Y. Zheng, S. Lv, Q. Wu, Y. Song, S. Zhao, Y. Zheng, T. Xin, Y. Wang, W. Wei, X. Ren, J. Yang, C. Ge, J. Tao, Y. Cheng, and H. Lyu, *Device*, 2023, **1**, 100004.
- 50 B. Prasad, V. Thakare, A. Kalitsov, Z. Zhang, B. Terris, and R. Ramesh, *Adv Electron Mater*, 2021, **7**, 2001074.
- 51 H. Wang, Z. Guan, J. Li, Z. Luo, X. Du, Z. Wang, H. Zhao, S. Shen, Y. Yin and X. Li, *Advanced Materials*, 2024, **36**, 2211305.
- 52 S. Wu, R. Cao, H. Jiang, Y. Li, X. Zhang, Y. Yang, Y. Wang, Y. Wei, and Q. Liu, *J. Semicond*, 2024, **45**, 032301.
- 53 M. Sowinska, T. Bertaud, D. Walczyk, S. Thiess, M. A. Schubert, M. Lukosius, W. Drube, Ch. Walczyk, and T. Schroeder, *Appl. Phys. Lett.*, 2012, **100**, 233509.
- 54 P. Calka, M. Sowinska, T. Bertaud, D. Walczyk, J. Dabrowski, P. Zaumseil, C. Walczyk, A. Gloskovskii, X. Cartoixa, J. Suñé, and T. Schroeder, *ACS Appl. Mater. Interfaces*, 2014, **6**, 5056.
- 55 M. Pešić, F. P. Gustav Fengler, L. Larcher, A. Padovani, T. Schenk, E. D. Grimley, X. Sang, J. M. LeBeau, S. Slesazek, U. Schroeder and T. Mikolajick, *Adv. Func. Mater.* 2016, **26**, 4601.
- 56 A. Chanthbouala, V. Garcia, R. O. Cherifi, K. Bouzehouane, S. Fusil, X. Moya, S. Xavier, H. Yamada, C. Deranlot, N. D. Mathur, M. Bibes, A. Barthélémy and J. Grollier, *Nat Mater*, 2012, **11**, 860–864.
- 57 M.-C. Nguyen, K. K. Min<sup>2†</sup>, W. Shin, J. Yim, R. Choi, and D. Kwon, *Nano Convergence*, 2025, **12**, 17.
- 58 N. Tasneem, H. Kashyap, K. Chae, C. Park, P.-C. Lee, S. F. Lombardo, N. Afroze, M. Tian, H. Kumarasubramanian, J. Hur, H. Chen, W. Chern, S. Yu, P. Bandaru, J. Ravichandran, K. Cho, J. Kacher, A. C. Kummel, and A. I. Khan, *ACS Appl. Mater. Interfaces*, 2022, **14**, 43897.
- 59 R. Marquardt, D. Petersen, O. Gronenberg, F. Zahari, R. Lamprecht, G. Popkrov, J. Carstensen, L. Kienle and H. Kohlstedt, *ACS Appl. Electron. Mater.* 2023, **5**, 3251.
- 60 M. D. Henry, D. Stoltzfus, M. K. Lenox, S. T. Jaszewski, T. Young, J. F. Ihlefeld, *J Appl Phys*, 2025, **137**, 144104.
- 61 K. McKenna, A. Shluger, V. Iglesias, M. Porti, M. Nafria, M. Lanza and G. Bersuker, *Microelectron Eng*, 2011, **88**, 1272–1275.



- 62 S. Boyn, A. M. Douglas, C. Blouzon, P. Turner, A. Barthélémy, M. Bibes, S. Fusil, J. M. Gregg and V. Garcia, *Appl Phys Lett*, 2016, **109**, 232902.

View Article Online  
DOI: 10.1039/D5NR04010H





### Data availability

Detailed electrical characterization results are shown in the ESI†.

